

NATIONAL AERONAUTICS AND SPACE ADMINISTRATION

*Technical Report No. 32-1012*

*High-Amplitude Dynamic-Stability  
Characteristics of Blunt  
10-Degree Cones*

*Robert H. Prislin*

FACILITY FORM 602

**N67 10254**

(ACCESSION NUMBER)

*21*

(PAGES)

*CR-79320*

(NASA CR OR TMX OR AD NUMBER)

(THRU)

(CODE)

*01*

(CATEGORY)

GPO PRICE \$ \_\_\_\_\_

CFSTI PRICE(S) \$ \_\_\_\_\_

Hard copy (HC) *1.00*

Microfiche (MF) *1.50*

ff 853 July 65

**jpl**

**JET PROPULSION LABORATORY  
CALIFORNIA INSTITUTE OF TECHNOLOGY  
PASADENA, CALIFORNIA**

October 15, 1966

NATIONAL AERONAUTICS AND SPACE ADMINISTRATION

*Technical Report No. 32-1012*

*High-Amplitude Dynamic-Stability  
Characteristics of Blunt  
10-Degree Cones*

*Robert H. Prislin*

Approved by:

A handwritten signature in dark ink, appearing to read 'E. A. Laumann', is written over a horizontal line.

E. A. Laumann, Manager  
Aerodynamic Facilities Section

JET PROPULSION LABORATORY  
CALIFORNIA INSTITUTE OF TECHNOLOGY  
PASADENA, CALIFORNIA

October 15, 1966

Copyright © 1966  
Jet Propulsion Laboratory  
California Institute of Technology  
Prepared Under Contract No. NAS 7-100  
National Aeronautics & Space Administration

## CONTENTS

<b>I. Introduction</b> . . . . .	1
<b>II. Testing Techniques and Models</b> . . . . .	2
A. Free-Flight Technique . . . . .	2
B. Free-Oscillation Technique . . . . .	2
C. Models . . . . .	4
<b>III. Data Reduction</b> . . . . .	4
A. Drag . . . . .	4
B. Static Stability . . . . .	5
C. Dynamic Stability . . . . .	5
D. Data Correlation Parameter . . . . .	6
<b>IV. Results and Discussion</b> . . . . .	6
A. Dynamic Stability (Amplitude and Nose Bluntness Effects) . . . . .	6
B. Dynamic Stability (Center-of-Gravity and Mach-Number Effects). . . . .	9
C. Dynamic Stability (Reynolds-Number Effects) . . . . .	11
D. Drag and Static Stability . . . . .	12
<b>V. Summary of Results</b> . . . . .	15
<b>Nomenclature</b> . . . . .	16
<b>References</b> . . . . .	16

## TABLE

1. Physical properties of test models . . . . .	4
---	---

## FIGURES

1. Typical free-flight sequence. . . . .	3
2. Test configurations and nomenclature . . . . .	4
3. Basic free-flight dynamic-stability: Plot A . . . . .	6
4. Basic free-flight dynamic-stability data: Plot B . . . . .	6
5. Basic free-flight dynamic-stability data: Plot C . . . . .	7

## FIGURES (Cont'd)

6. Basic free-flight dynamic-stability data: Plot D . . . . .	7
7. Basic free-flight dynamic-stability data: Plot E . . . . .	7
8. Basic free-oscillation dynamic-stability data: Plot A . . . . .	7
9. Basic free-oscillation dynamic-stability data: Plot B . . . . .	7
10. Basic free-oscillation dynamic-stability data: Plot C . . . . .	8
11. Basic free-oscillation dynamic-stability data: Plot D . . . . .	8
12. Basic free-oscillation dynamic-stability data: Plot E . . . . .	8
13. Basic free-oscillation dynamic-stability data: Plot F . . . . .	8
14. Basic free-oscillation dynamic-stability data: Plot G . . . . .	8
15. Effects of oscillation amplitude on dynamic stability . . . . .	9
16. Comparison of free-flight and free-oscillation data . . . . .	9
17. Effects of nose bluntness on dynamic stability . . . . .	9
18. Effects of center-of-gravity location on dynamic stability: Sharp cone . . . . .	9
19. Effects of center-of-gravity location on dynamic stability: Blunted cone . . . . .	10
20. Effects of Mach number on dynamic stability: Sharp cone . . . . .	10
21. Effects of Mach number on dynamic stability: Blunted cone . . . . .	11
22. Effects of Reynolds number on dynamic stability: Plot A . . . . .	11
23. Effects of Reynolds number on dynamic stability: Plot B . . . . .	11
24. Free-flight drag data: Sharp cone . . . . .	12
25. Free-flight drag data: Blunted cone . . . . .	12
26. Effects of nose bluntness on drag . . . . .	12
27. Effects of nose bluntness and Mach number on drag . . . . .	12
28. Free-flight static-stability data: Plot A . . . . .	13
29. Free-flight static-stability data: Plot B . . . . .	13
30. Free-oscillation static-stability data: Plot A . . . . .	13
31. Free-oscillation static-stability data: Plot B . . . . .	14
32. Free-oscillation static-stability data: Plot C . . . . .	14
33. Free-oscillation static-stability data: Plot D . . . . .	14
34. Free-oscillation static-stability data: Plot E . . . . .	14
35. Free-oscillation static-stability data: Plot F . . . . .	14
36. Effects of Reynolds number on static stability: Plot A . . . . .	14
37. Effects of Reynolds number on static stability: Plot B . . . . .	15

## ABSTRACT

An extensive investigation of the dynamic-stability characteristics of a family of spherically blunted  $10^\circ$  cones has been conducted in the Jet Propulsion Laboratory (JPL) supersonic and hypersonic wind-tunnels. Two testing techniques were employed (1) the free-flight technique (2) the captive free-oscillation technique. Parameters considered include center-of-rotation, oscillation-amplitude, Mach-number, and Reynolds-number. There were several major trends observed in the test results. For the very blunt shapes, dynamic stability was insensitive to changes in both oscillation amplitude and Mach number; however for a sharp cone, a large change was evident for variations in both Mach number and amplitude. As the Mach number increased from low to high supersonic, the dynamic stability decreased. As the Mach number continued to increase into the hypersonic regime, this trend reversed itself and the sharp cone became more stable. Variations in Reynolds number have a significant effect on dynamic-stability coefficients. The magnitude of this effect decreases with increasing model nose bluntness, oscillation amplitude, and Mach number. At the higher Mach numbers, correlation between results obtained with the alternate testing techniques is excellent. But, at the lower Mach numbers ( $M = 2$ ) the agreement is less satisfactory, mainly because of scatter and poor quality of the captive data.

## 1. INTRODUCTION

During some phases of atmospheric entry, aerodynamic dynamic-stability coefficients may have a dominant effect in the determination of the oscillatory-amplitude history of a vehicle. However, large amplitude experimental data on blunt configurations, particularly in free-flight, are almost nonexistent. This paper presents the results of an extensive wind-tunnel investigation conducted at JPL on the dynamic-stability characteristics of a family of spherically blunted 10-deg half-angle cones.

To date, most wind-tunnel dynamic-stability studies have employed either a sting-supported forced oscilla-

tion, or a sting or cross-supported free-oscillation technique. Usual evaluation of data from these captive-type tests tends toward the assumption that support interference effects are negligible. The results may be subject to question, because of this assumption. In addition, these techniques (with the exception of the cross-supported free-oscillation technique) generally restrict model oscillatory motion to relatively low amplitudes. Therefore, in order to eliminate an amplitude restriction and to insure the validity of the results of this investigation, the bulk of the data were obtained by means of a wind-tunnel free flight technique. Supplemental data were taken

using a sting-supported free-oscillation technique. Consequently, as an additional product of this test program, definitive comparisons between captive and support-free results are available.

The nose-bluntness radii ratioed to the base radii for the models tested ranged from 0.0 to 0.846. Oscillation amplitudes varied between 0 and 80 deg for the free-flight testing and between 0 and 25 deg for the free-oscillation technique. The primary investigation was conducted at a free-stream Mach number of 4.0, but data were also taken at Mach numbers ranging from 2.0 to 10.0. Other parameters investigated were Reynolds-number and center-of-gravity location. Both static and dynamic sta-

bility, as well as drag (free-flight runs only) were determined for the family of configurations.

The approach taken was to thoroughly document one particular Mach number and Reynolds number over a range of nose-bluntness ratios and oscillation amplitudes with the free-flight technique. In additional free-flight runs, Mach number and center-of-gravity location were varied for fixed nose-bluntness ratios. The free-oscillation runs consisted of a Reynolds-number survey for the sharper configurations and a Mach-number survey for the bluntest shape. From the data obtained, it is possible to make reliable dynamic-stability predictions for any combination of the parameters within the ranges considered.

## II. TESTING TECHNIQUES AND MODELS

### A. Free-Flight Technique

The free-flight models were launched against the air-stream with a pneumatic launcher located downstream of the test section viewing window (Ref. 1). The release point was far enough downstream (6 to 10 in.) so that the model wakes were free from any influence of the projecting mechanism during the viewable trajectory.

For initial angles of attack up to 30 deg, the models were mounted on a horizontal wedge fitting within the model base. At higher initial angles of attack, a cradle support, contoured to the model base and side, was used. Both of these support methods generally resulted in planar, oscillatory motion, simplifying the data reduction. By properly balancing the launcher chamber pressure and the model aerodynamic acceleration, the model can be made to approach the upstream edge of the viewing window, stop, and travel downstream. For the models tested, this trajectory resulted in 5 to 10 oscillation cycles at frequencies on the order of 60 cps. The motion was recorded with a 35-mm half-frame motion-picture camera operating at about 5000 frames/sec. The photographs were taken through the wind-tunnel schlieren system, thereby eliminating parallax distortions and providing a flow-visualization history. A high-speed motion-picture sequence is shown in Fig. 1.

### B. Free-Oscillation Technique

The free-oscillation technique used a model mounted in the wind-tunnel on an airbearing, free to oscillate in one plane. The maximum model-angular excursion was limited by the sting and the model base to a range from 20 deg (sharp cone) to 45 deg (blunt cone). The model was pitched to its maximum angle of attack, released, and allowed to oscillate freely until damped by the bearing friction and the aerodynamics. The damping due to the bearing friction is normally measured with a calibration sphere prior to the recording of the data. The sphere, mounted on a diameter, contains an offset mass to provide a restoring moment. Since the aerodynamic effects are small, as a sphere oscillates about a diameter, the angular history provides a measure for the tare damping. This term is less than 0.1% of the aerodynamic damping of a sharp cone and, in general, can be ignored. The data were collected with an Optron Tracker<sup>1</sup>, a passive optical-electronic device designed to follow the motion of an object without physical contact. The output of this device is a continuous analog record of the model angle of attack vs time. Further detail on both testing techniques may be found in Ref. 2.

<sup>1</sup>Manufactured by the Optron Corporation, Santa Barbara, California.

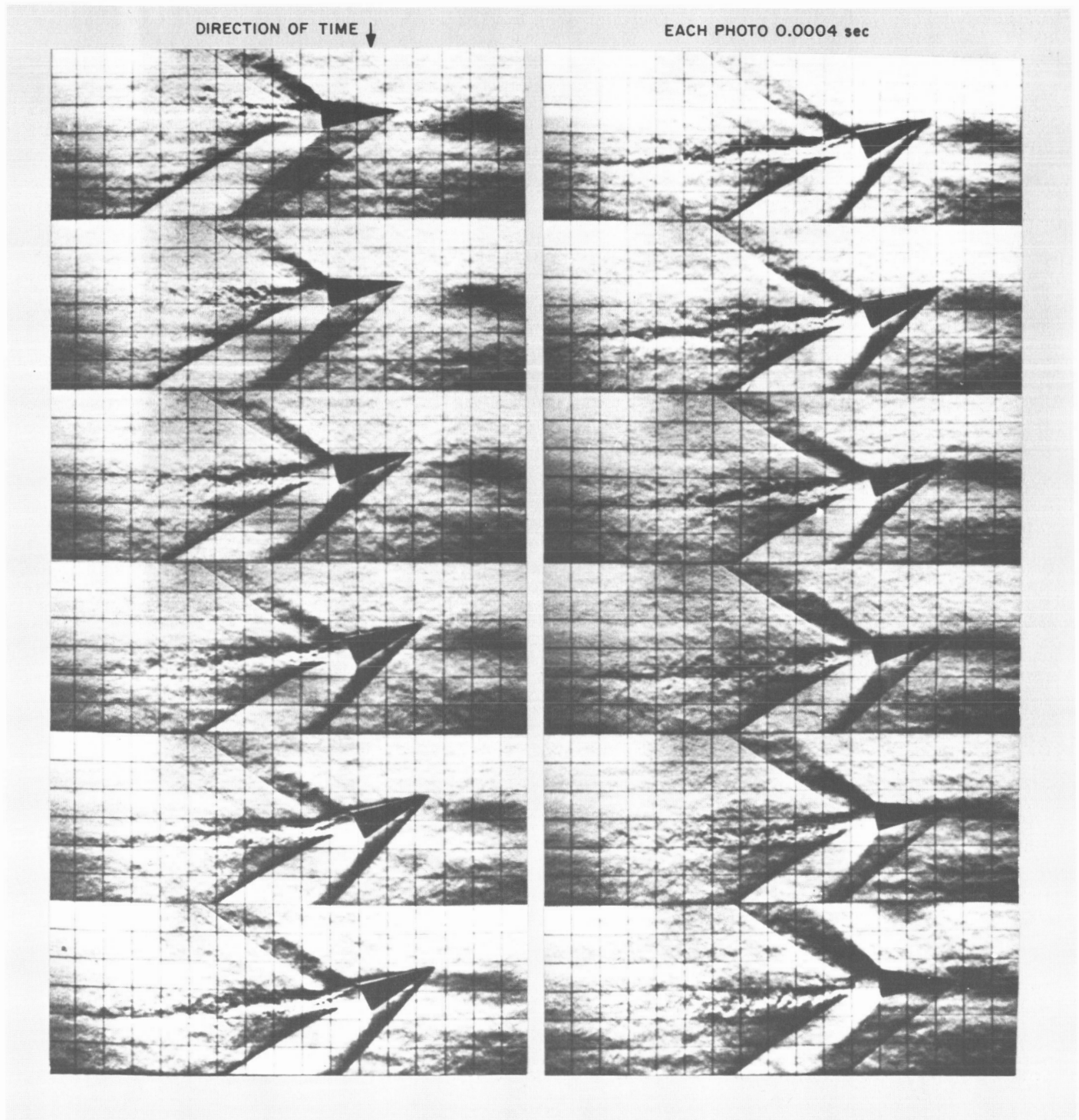


Fig. 1. Typical free-flight sequence



### C. Models

Sketches of representative model configurations and the nomenclature used are shown in Fig. 2. For all shapes, the center-of-gravity location is referenced in lengths of a hypothetical sharp cone aft of the hypothetical sharp nose. The free-flight models were made of a thin shell of either polystyrene plastic, or magnesium and a lead ballast. The free-oscillation models are con-

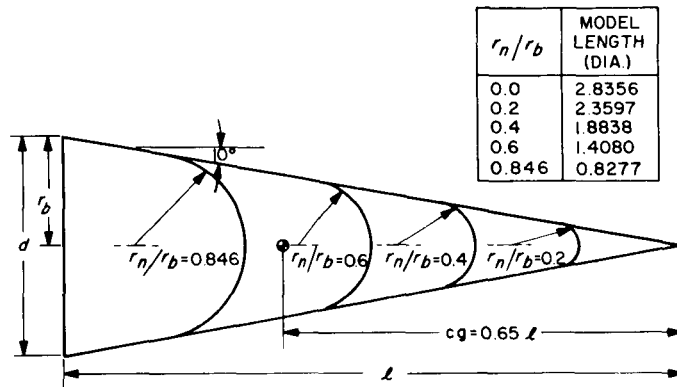


Fig. 2. Test configurations and nomenclature

structed of thin-shell stainless steel, or electrolytic nickel. Physical characteristics for both free-flight and free-oscillation models are given in Table 1.

Table 1. Physical properties of test models

$r_n/r_b$	Diam, in.	Mass slugs	$I$ slug-ft <sup>2</sup>	$cg/\ell$	$\omega d/V \times 10^2$
<b>A. Free oscillation</b>					
0.0	5.25	—	$6 \times 10^{-2}$	0.604–0.662	0.21–0.95
0.182	5.25	—	$5 \times 10^{-2}$	0.604–0.662	0.33–1.22
0.188	5.10	—	$5 \times 10^{-2}$	0.606–0.665	0.17–0.53
0.400	5.25	—	$5 \times 10^{-2}$	0.604–0.662	0.36–1.22
0.846	4.00	—	$3 \times 10^{-1}$	0.85	0.07–1.40
<b>B. Free flight</b>					
0.0	1.00	$1 \times 10^{-3}$	$1 \times 10^{-11}$	0.494–0.620	0.94–1.99
0.188	0.50	$2 \times 10^{-4}$	$4 \times 10^{-11}$	0.480–0.590	0.57–1.19
0.200	1.00	$1 \times 10^{-3}$	$1 \times 10^{-11}$	0.460–0.610	1.44
0.400	1.00	$2 \times 10^{-3}$	$1 \times 10^{-11}$	0.600–0.700	1.13
0.600	1.00	$2 \times 10^{-3}$	$1 \times 10^{-11}$	0.650–0.700	1.19
0.846	1.00	$2 \times 10^{-3}$	$6 \times 10^{-11}$	0.85	1.18

## III. DATA REDUCTION

The raw data from free-flight and free-oscillation techniques consisted of time, translational position, and angle-of-attack history of the model. The free-flight data reduction will be described briefly here. A similar approach may be used on the free-oscillation data, but simplified by the elimination of translational motion. Reference 2 contains a complete derivation of the data reduction equations for both techniques.

### A. Drag

The coordinate system used throughout the data reduction references the model's position to the moving gas media.  $X$  is the distance between the model and the media and is the independent variable for the equations

of motion. The basic equation from which the drag coefficient was determined is

$$m\ddot{X} = \frac{1}{2}\rho V^2 AC_D \quad (1)$$

Changing the independent variable from time to distance yields the following solution for the drag coefficient

$$C_D = -\frac{2m}{\rho A} \frac{d(\ln V)}{dX} \quad (2)$$

A linear curve fit through a section of the  $\ln V$  vs  $X$  data yields an effective constant drag coefficient for that section. This effective constant coefficient will, of course,

vary with the oscillation amplitude. A drag vs angle of attack curve may be derived from these data by noting that the effective coefficient at a given amplitude equals a distance-averaged integral of the local curve over an oscillation cycle.

### B. Static Stability

The solution to the linearized equation of planar angular motion (i.e., linear aerodynamic coefficients  $C_m = C_{m_a}\alpha$ ,  $C_L = C_{L_a}\alpha$ ,  $C_D = C_{D_0}$ ) is well known

$$\alpha = \alpha_0 e^{\lambda x} \cos \left[ \left( \frac{-\rho A d}{2I} C_{m_a} + \lambda^2 \right)^{1/2} X \right] \quad (3)$$

where

$$\lambda = \frac{\rho A}{4m} \left[ C_{D_0} - C_{L_a} + \frac{md^2}{I} \{ C_{m_q} + C_{m_a} \} \right]$$

In general,  $(-\rho A d / 2I) C_{m_a} \gg \lambda^2$  and therefore an effective constant pitching moment slope is given by

$$C_{m_{a(eff)}} = - \frac{2I\Omega^2}{\rho A d} \quad (4)$$

where  $\Omega$  is the distance frequency of oscillation. Deviations of  $C_{m_{a(eff)}}$  from a constant value as the oscillation amplitude varies are a direct measure of the nonlinearity of the actual pitching moment. A method for determining the coefficients of an assumed nonlinear functional form of the pitching moment from  $C_{m_{a(eff)}}$  vs oscillation-amplitude data is developed in Ref. 2. Since the pitching moment is the dominant term determining the oscillatory frequency and amplitude history of a vehicle (over a short enough time period so that the amplitude decay remains relatively small) a linear effective curve vs amplitude is uniquely representative of the true nonlinear moment. The static-stability coefficients presented in this report are effective constant coefficients calculated with Eq. (4).

### C. Dynamic Stability

The dynamic-stability coefficient may be obtained from Eq. (3) in terms of the amplitude envelope

$$\{ C_{m_q} + C_{m_a} \} \frac{md^2}{I} = \frac{4m}{\rho A} \frac{1}{X} \ln \frac{\alpha_x}{\alpha_0} + C_{L_a} - C_{D_0} \quad (5)$$

However, the consequences of the linearizing assumptions on this solution are not in general tolerable for the

configurations investigated in this program. The fact that the dynamic-stability coefficient is itself a second order effect implies that terms unimportant or negligible in a static-stability analysis are not necessarily insignificant here. This fact becomes clearer upon consideration of the following two points: (1) Lift and drag may account for from 10 to 40% of the amplitude decay; therefore, using linear approximations of these coefficients may result in a considerable loss of accuracy in the dynamic-stability coefficient. (2) The use of an effective constant pitching moment slope in place of the nonlinear moment matches the oscillation frequency and amplitude. However, the angular velocity, which appears as a multiplication factor of  $\{ C_{m_q} + C_{m_a} \}$  in the differential equation of motion, may vary considerably over an oscillation cycle (though it would be identical at end points) when comparing the motion corresponding to the nonlinear moment and the equivalent linear moment. Thus, the energy dissipation over a cycle, which is equivalent to an amplitude decay, could be quite different in the two cases even with identical damping coefficients. Therefore, calculations of dynamic-stability coefficients from amplitude decay using the linear solution could be significantly in error. Furthermore, in contrast to the static-stability analysis a  $\{ C_{m_q} + C_{m_a} \}$  vs amplitude curve so obtained would not necessarily be representative of a particular nonlinear situation.

A general approach to the problem which will account for nonlinear aerodynamics is developed in Ref. 2. The two primary assumptions made in this solution are that the pitching moment is the dominant factor in the motion determination and that the damping coefficient is effectively constant. The approach used is to solve the equation of motion with the desired nonlinear pitching moment assuming a constant velocity (zero lift and drag) and no damping. Generally, an exact solution may be found in terms of elliptic functions. This exact solution is then used to determine the effects of lift, drag, and damping. The second solution will be a small perturbation of the first exact solution. Further iterations along the same line could be carried out, but in a typical physical situation they are not necessary. For simpler forms of nonlinear pitching moments (e.g., a cubic pitching moment) the damping coefficient may be expressed as the product of the linear solution and a correction factor based on the nonlinear coefficients and the oscillation amplitude. This correction factor needs to be calculated only once as a function of properly normalized nonlinear coefficients and the oscillation amplitude for any particular nonlinear form. Thus, the actual solution is very easy to apply.

For this program the aerodynamic coefficients were assumed to have the following functional forms  $C_D = C_{D_0} + b_1\alpha^2 + b_2\alpha^4$ ;  $C_L = C_{L_0}\alpha + c_1\alpha^3 + c_2\alpha^5$ ;  $C_m = C_{m_0}\alpha + 2r_m\alpha^3$ . The data included in this report show that these approximations are excellent.

#### D. Data Correlation Parameter

The correction terms which account for the nonlinear aerodynamics are based on an oscillation-amplitude value which changes during the flight due to the decay. It is therefore necessary to define a distance-averaged

amplitude value to be used in the calculations and for data correlation. Assuming a constant decay which is small in comparison with the oscillation frequency the mean amplitude  $\bar{\alpha}_0$  will be defined as

$$\bar{\alpha}_0^2 \equiv \frac{\int_0^x \alpha^2 dX}{X} = \frac{\alpha_x^2 - \alpha_0^2}{2 \ln \frac{\alpha_x}{\alpha_0}} \quad (6)$$

Note that in the limit as the decay approaches zero,  $\bar{\alpha}_0 = \alpha_0$ .

### IV. RESULTS AND DISCUSSION

#### A. Dynamic Stability (Amplitude and Nose Bluntness Effects)

The basic dynamic-stability vs amplitude data for all configurations are presented in Figs. 3-14. Figures 3-7 (the sharp cone data in Fig. 4 previously appeared in Ref. 3) are free-flight data and Figs. 8-14 are free-oscillation data. For comparison purposes, some of the free-flight data are summarized in Fig. 15. The free-stream flow conditions were identical for all the data in this figure, Mach 4.0 and Reynolds number  $0.29 \times 10^6$ . The same general trend appears in all of these curves; the coefficient remains fairly constant at the low amplitudes

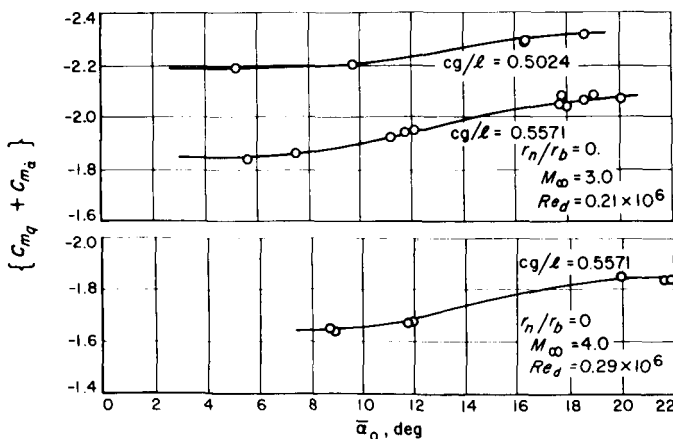


Fig. 3. Basic free-flight dynamic-stability data: Plot A

and begins to increase negatively rather sharply, indicating greater dynamic stability, at an amplitude near the cone semi-vertex angle. As the envelope angle continues to increase, the rise becomes more gradual, and the stability derivatives appear to approach a new level at the higher amplitudes. The abrupt increase in dynamic stability at an amplitude near the cone half-angle may be associated with flow separation on the lee side of the body. As the cone is pitched to an angle-of-attack, some

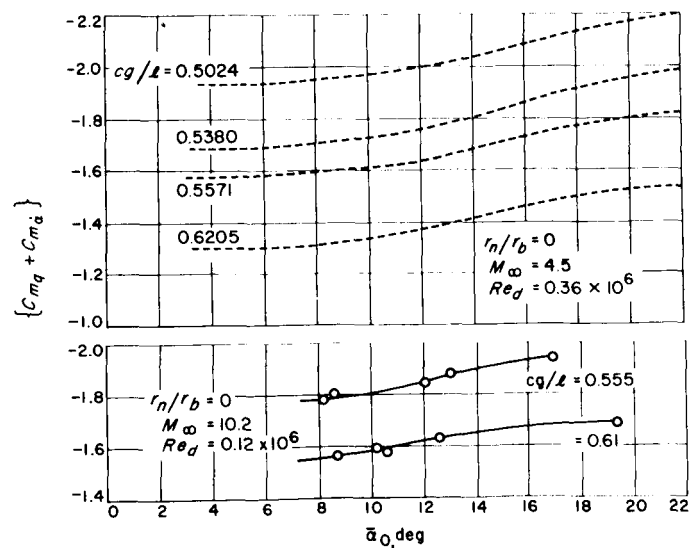


Fig. 4. Basic free-flight dynamic-stability data: Plot B

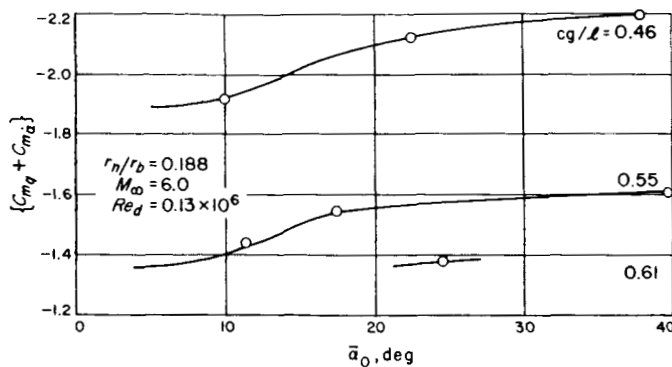


Fig. 5. Basic free-flight dynamic-stability data: Plot C

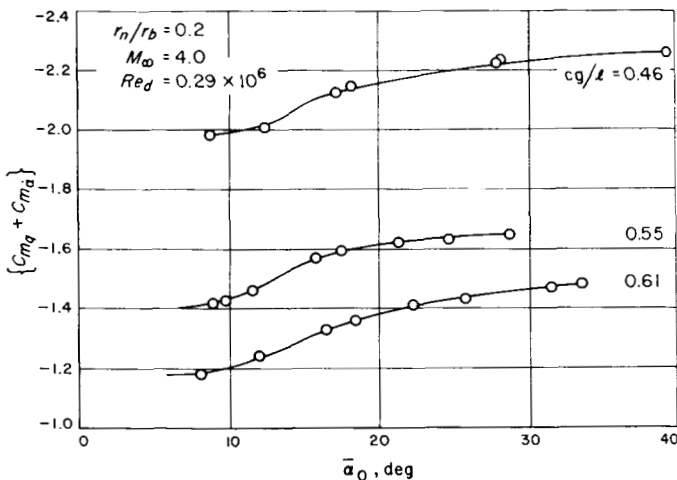


Fig. 6. Basic free-flight dynamic-stability data: Plot D

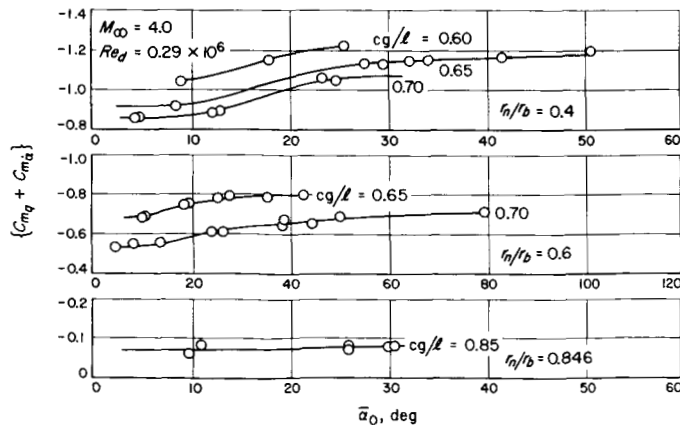


Fig. 7. Basic free-flight dynamic-stability data: Plot E

of the flow entering the boundary layer on the windward side is conveyed toward the lee side boundary layer by a strong circumferential pressure gradient. Eventually this influx of flow can no longer be accommodated on the lee side, and flow separation occurs at about the cone half-angle (Ref. 4). This results in an increase in the pressure differential between the two sides of the cone and a corresponding increase in the energy dissipation, hence the damping coefficient. As the oscillation amplitude continues to increase, the portion of an oscillation cycle when the flow is separated becomes more influential in the determination of an effective damping coefficient. As an example, for the sharp 10-deg cone at amplitudes above 25 deg this is the dominant factor and further amplitude change has little effect.

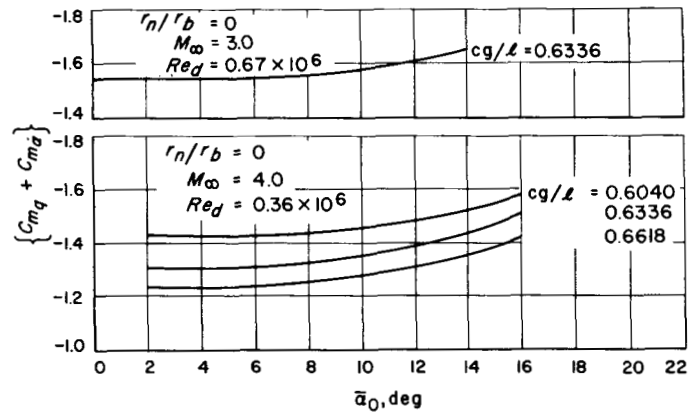


Fig. 8. Basic free-oscillation dynamic-stability data: Plot A

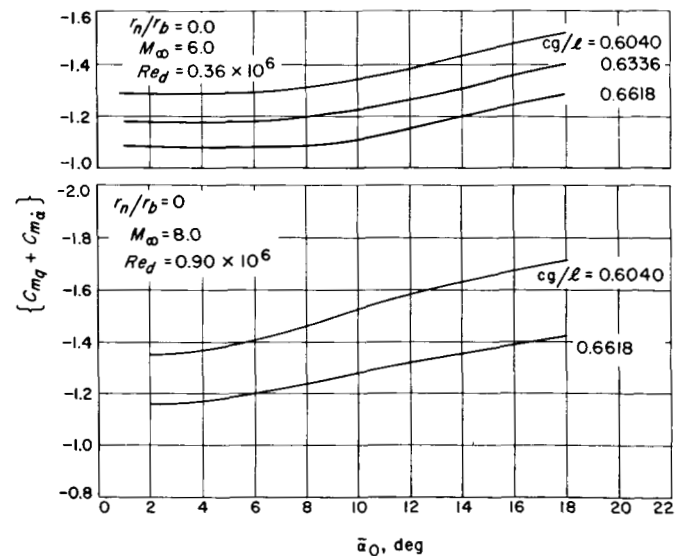


Fig. 9. Basic free-oscillation dynamic-stability data: Plot B

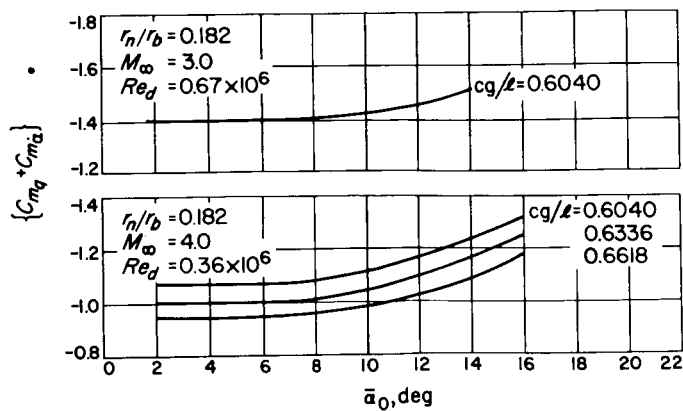


Fig. 10. Basic free-oscillation dynamic-stability data: Plot C

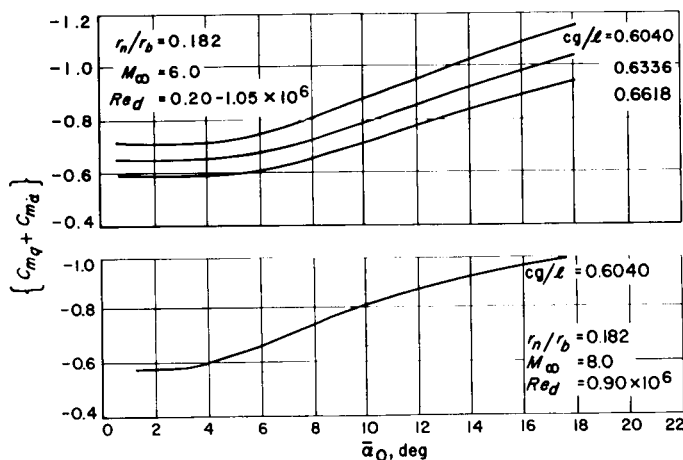


Fig. 11. Basic free-oscillation dynamic-stability data: Plot D

This trend of increasing dynamic stability with increasing amplitude becomes less pronounced as the nose bluntness ratio is increased. At this Mach number, for the sharp cone there is a 17% change in the coefficient as the amplitude goes from 2 to 20 deg, whereas for a cone with bluntness ratio 0.6, there is only a 10% change over the same amplitude range. For the bluntest configuration tested,  $r_n/r_b = 0.846$ , amplitude effects are no longer visible, the coefficient remaining virtually constant from 0 to 40 deg. These data presented on this summary plot are quite typical of free-flight data at other Mach numbers, all curves exhibiting similar shapes for corresponding nose bluntness ratios.

Figure 16 compares amplitude data for a blunt cone obtained with the two alternate testing techniques. The captive data generally begin to rise at a somewhat lower angle, at 4 to 8 deg amplitude, than do the free-flight

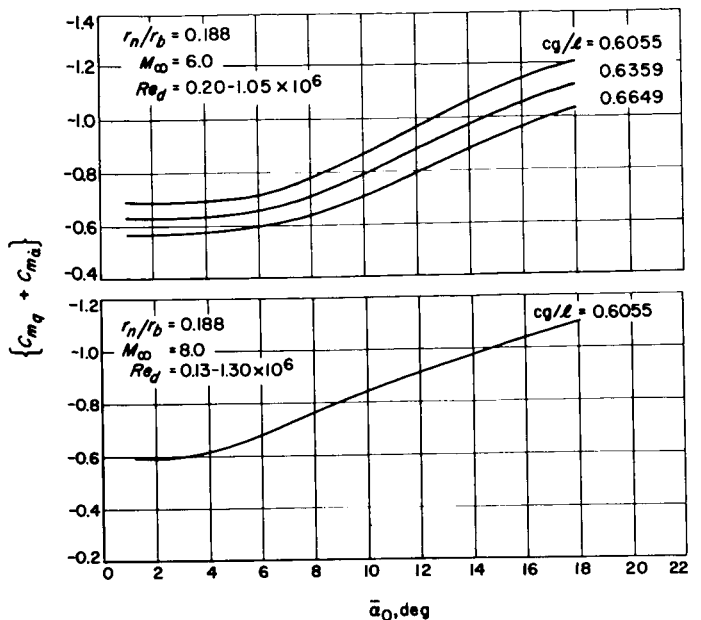


Fig. 12. Basic free-oscillation dynamic-stability data: Plot E

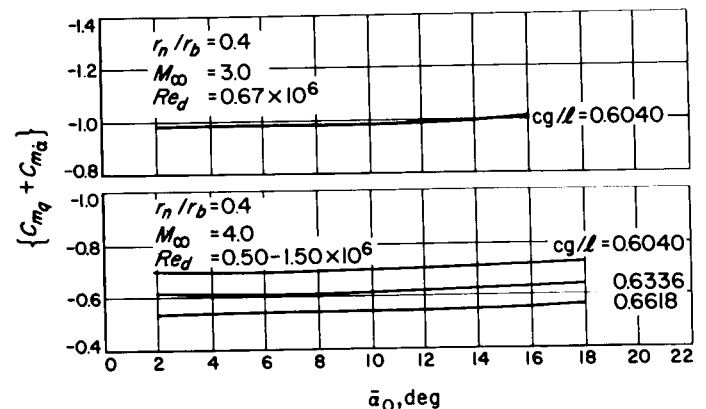


Fig. 13. Basic free-oscillation dynamic-stability data: Plot F

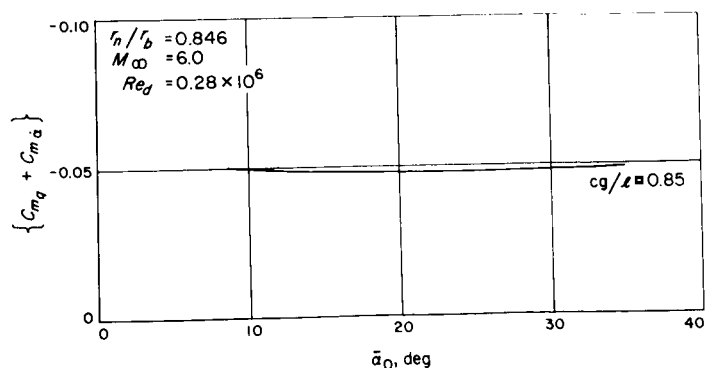


Fig. 14. Basic free-oscillation dynamic-stability data: Plot G

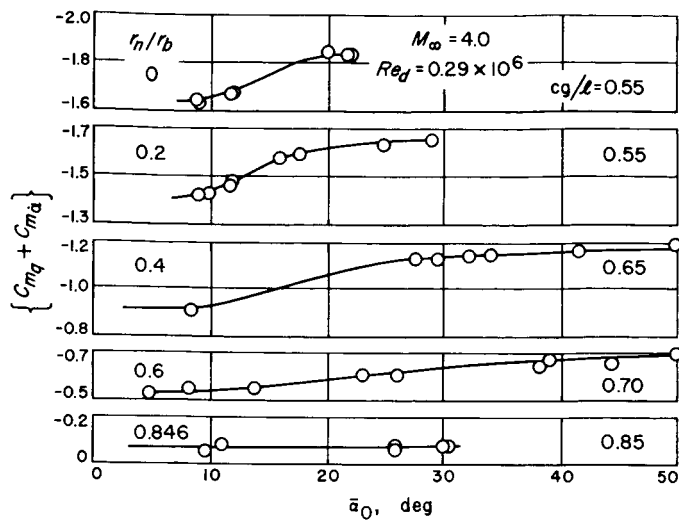


Fig. 15. Effects of oscillation amplitude on dynamic stability

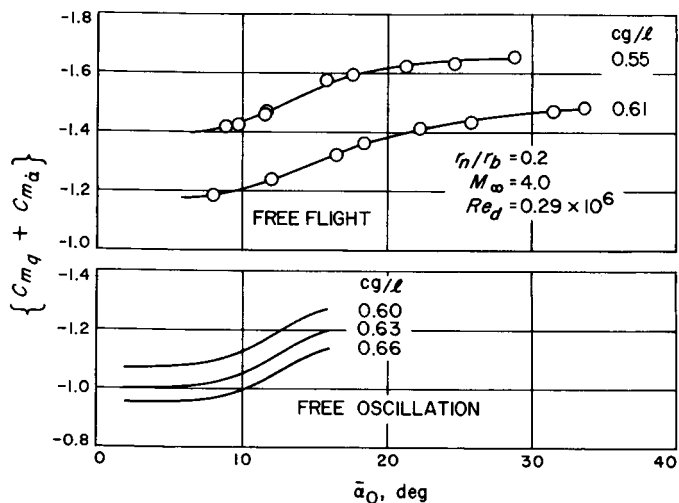


Fig. 16. Comparison of free-flight and free-oscillation data

data, 8 to 10 deg, but thereafter the curves appear to remain parallel. The agreement between the two techniques is quite good, and validates a generalization of the observed characteristic shape of a dynamic-stability versus oscillation-amplitude curve to similar configurations.

The effects of the nose bluntness ratio for several fixed-oscillation amplitudes are compared with a zero angle-of-attack curve calculated from the Newtonian impact theory in Fig. 17. The data are all free-flight data taken at a free-stream Mach 4.0. The experimental values for the sharp cone are substantially greater in magnitude

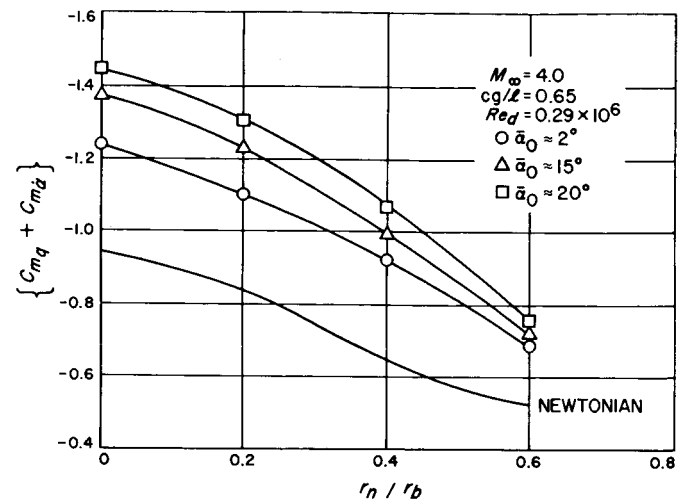


Fig. 17. Effects of nose bluntness on dynamic stability

than the Newtonian prediction; however, as the bluntness ratio increases the experimental curves at all amplitudes converge toward the Newtonian values. Experimental data at  $r_n/r_b = 0.846$ , not shown on this plot, agree quite well with the Newtonian theory, confirming the general trend. This figure also shows the equalizing effect of nose bluntness with regard to oscillation-amplitude effects. The spread between the different amplitude curves is considerably greater for a sharp cone than it is for a cone with bluntness ratio of 0.6.

## B. Dynamic Stability (Center-of-Gravity and Mach-Number Effects)

Figure 18 presents the effect of center-of-rotation on the dynamic-stability coefficient for the sharp cone. This

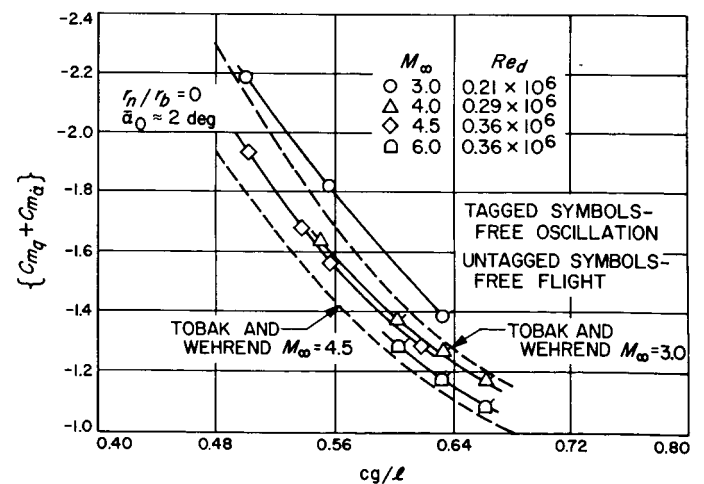


Fig. 18. Effects of center-of-gravity location on dynamic stability: Sharp cone

figure includes free-flight data taken at Mach 3.0, 4.0, and 4.5, and free-oscillation data taken at Mach 3.0, 4.0, and 6.0. The experimental curves are compared with Tobak and Wehrend's first and second order potential flow solution (Ref. 5). There is good agreement between the experimental data and the theory at all Mach numbers, the maximum deviation being about 8%. This plot also shows excellent correlation between the data obtained with the alternate testing techniques.

The same type of data for a blunt cone,  $r_n/r_b = 0.2$ , are shown in Fig. 19. The data were taken at Mach 4.0 and 6.0, using both testing techniques. The data are compared with a curve calculated with the Newtonian impact theory. The free-flight and free-oscillation curves exhibit the same shape; however, the levels of the curves differ significantly, with the free-oscillation coefficient smaller in magnitude than the free-flight coefficient. Data for a cone with bluntness ratio  $r_n/r_b = 0.4$ , not shown on a summary plot, exhibit the same characteristic with a similar discrepancy between the two techniques. No explanation for this inconsistency is apparent at this time. However, because of the abundance and repeatability of the free-flight data and the nature of the testing techniques (possible support interference effects) it is felt that the free-flight values are the more reliable of the two.

Under the assumption of linear (effective) aerodynamics, the dynamic-stability derivative obeys the center-of-gravity transformation equation

$$\{C_{m_q} + C_{m_{\dot{\alpha}}}\} = \{C_{m_q} + C_{m_{\dot{\alpha}}}\}_{nose} + \frac{cg}{d} (C_{N_q} + C_{N_{\dot{\alpha}}})_{nose} - \frac{cg}{d} \left( C_{m_a}_{nose} + \frac{cg}{d} C_{N_a} \right) \quad (7)$$

In this equation,  $cg/d$  is the center-of-gravity location in terms of diameters from the actual nose of the model, not from the nose of a hypothetical sharp cone. Tobak and Wehrend's potential flow solution, as well as the Newtonian theory, follows this transformation equation. In addition, all of the experimental results obtained fit this equation quite well. Though no data on center-of-gravity effects for the blunter shapes were taken, the observed trend can be extrapolated into this area. Thus, it can be concluded that for any given fixed-oscillation amplitude, linear effective aerodynamics in this transformation equation will yield an excellent prediction of center-of-gravity dependence. Assuming the static aerodynamics are known,  $(C_{N_q} + C_{N_{\dot{\alpha}}})_{nose}$  and  $\{C_{m_q} + C_{m_{\dot{\alpha}}}\}_{nose}$

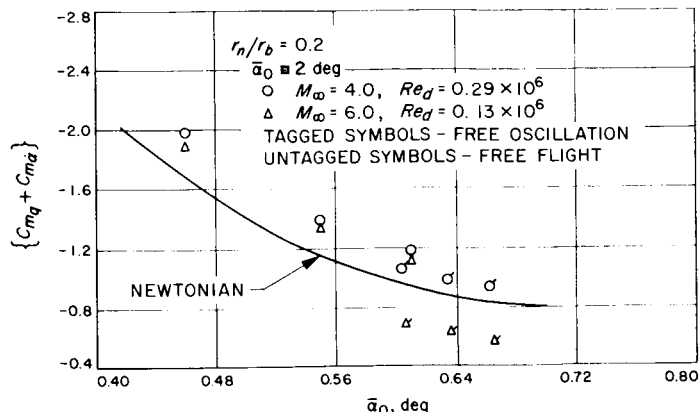


Fig. 19. Effects of center-of-gravity location on dynamic stability: Blunted cone

may be calculated from experimental data at two arbitrary center-of-gravity locations. These data may then be used to calculate  $\{C_{m_q} + C_{m_{\dot{\alpha}}}\}$  at any  $cg$  location.

The effect of Mach number on the dynamic-stability coefficient of a sharp cone is shown in Fig. 20. The data are compared with Tobak and Wehrend's solution in the supersonic regime and with a modified shock expansion solution (Ref. 6) in the hypersonic regime. The two theories adequately predict both the shape and level of the experimental curve with the maximum deviation being on the order of 8%. Both theory and experiment show a pronounced drop in dynamic stability as Mach number increases from low to high supersonic. The curve levels off in the Mach 4.0 to 6.0 region, and as the Mach number continues to increase above 8.0, dynamic stability increases. According to the shock expansion theory the dynamic stability should be a minimum at the Mach number where the Mach angle equals the cone half-angle. For a 10-deg cone this would be at Mach 5.76,

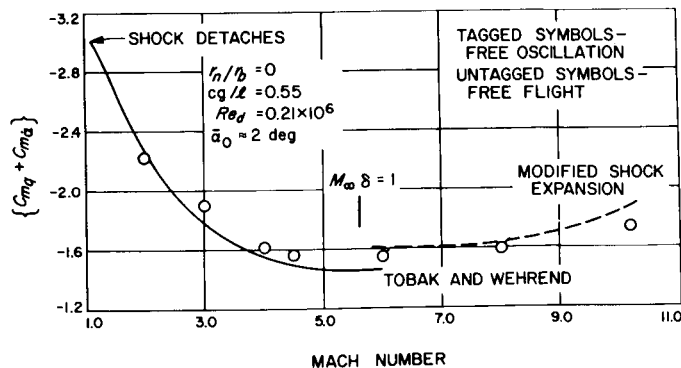


Fig. 20. Effects of Mach number on dynamic stability: Sharp cone

very close to the minimum indicated by the experimental data.

Figure 21 presents  $\{C_{m_q} + C_{m_{\dot{\alpha}}}\}$  versus Mach number for a slightly blunted and a very blunted cone. Even for the slightly blunted cone, the effects of Mach number are greatly reduced as compared to the sharp cone case. For the very blunt cone, Mach number has little effect; the coefficient remains almost constant between Mach 2.0 and 8.0. The difference between Mach number effects for the sharp and blunted cones may be explained as follows. The sharp cone has an attached bow shock and therefore the flow along the cone surface is supersonic. A change in the free-stream Mach number will result in corresponding changes in the flow on the cone surface, and in the aerodynamic forces and moments acting on a body. However, for the blunt cone the bow shock is detached, and the flow behind the shock is subsonic. This detached shock is the dominant characteristic of the flow field and is not greatly affected by changes in the free-stream Mach number. Therefore, the aerodynamic coefficients also reflect no significant influence of Mach number.

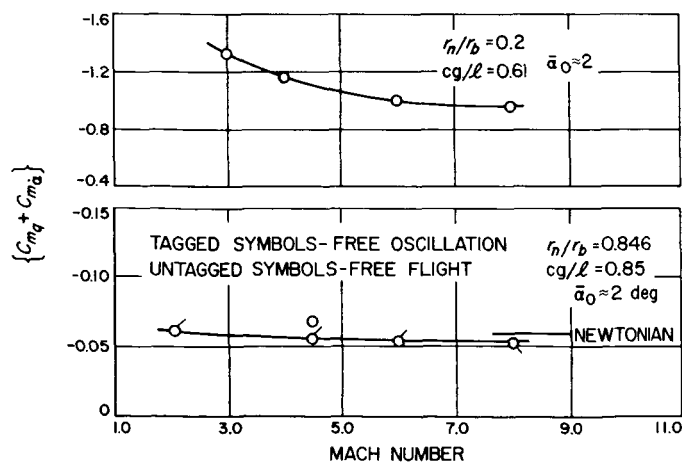


Fig. 21. Effects of Mach number on dynamic stability: Blunted cone

### C. Dynamic Stability (Reynolds-Number Effects)

Brief Reynolds number surveys were taken at Mach 4.0, 6.0 and 8.0, using only the free-oscillation technique. Figures 22-23 present the dynamic-stability coefficient plotted vs Reynolds number. In each plot the lower curves represent an oscillation amplitude of 2 deg while the upper curves are for an amplitude of 15 deg. For all configurations and Mach numbers tested, a Reynolds number effect was apparent only at the lower oscillation

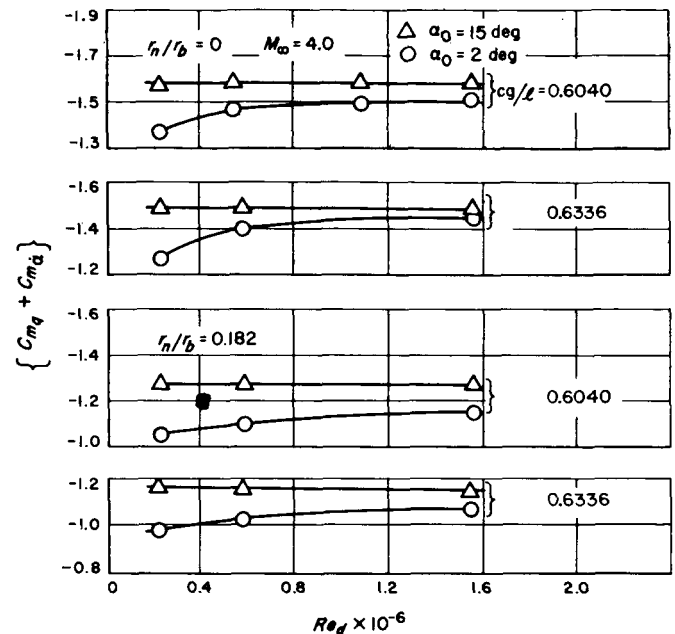


Fig. 22. Effects of Reynolds number on dynamic stability: Plot A

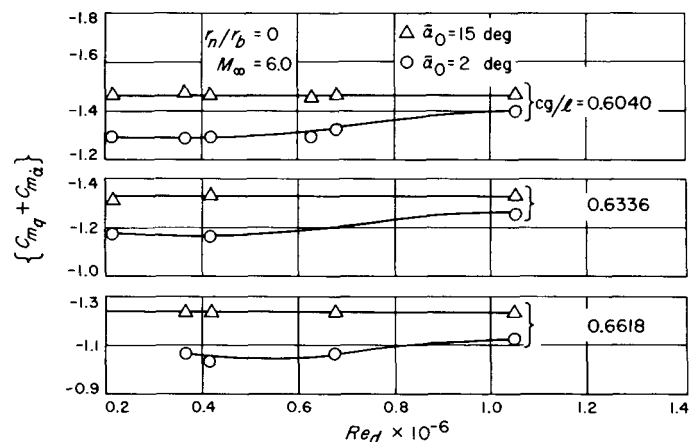


Fig. 23. Effects of Reynolds number on dynamic stability: Plot B

amplitudes. At amplitudes above 12 to 15 deg the coefficients remained constant with Reynolds number. Figure 22 shows data for a sharp and slightly blunted cone at a free-stream Mach 4.0. The effect on the blunt cone is less in magnitude than that for the sharp cone. Over the Reynolds number range tested, the sharp cone coefficient varies about 12% while the blunt cone varies only about 7%. Further blunting of the model nose extends the pattern of a decreasing Reynolds number effect. For a cone with bluntness ratio of 0.4, the experimental data showed no Reynolds number effects at this Mach number.



Figure 23 shows the damping coefficient vs. Reynolds number for a sharp cone at a free-stream Mach 6.0. The variation in the coefficient with Reynolds number over the range tested is about 8%, which is less than the variation for the same configuration at Mach 4.0. Blunting the cone again caused a decrease in Reynolds number effects. In fact, at this Mach number for all of the

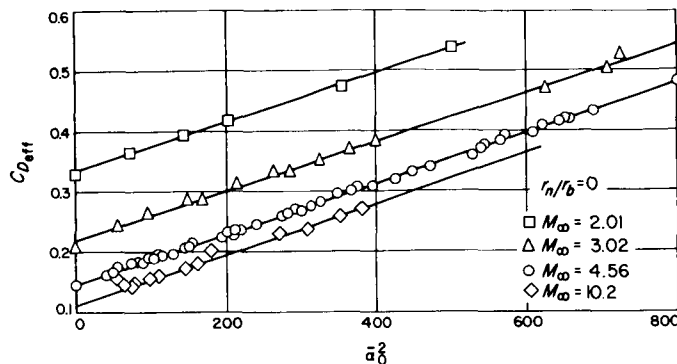


Fig. 24. Free-flight drag data: Sharp cone

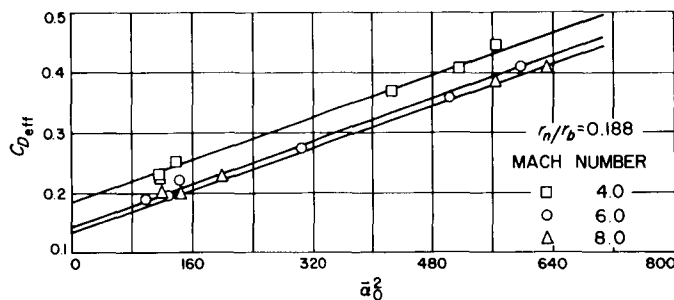


Fig. 25. Free-flight drag data: Blunted cone

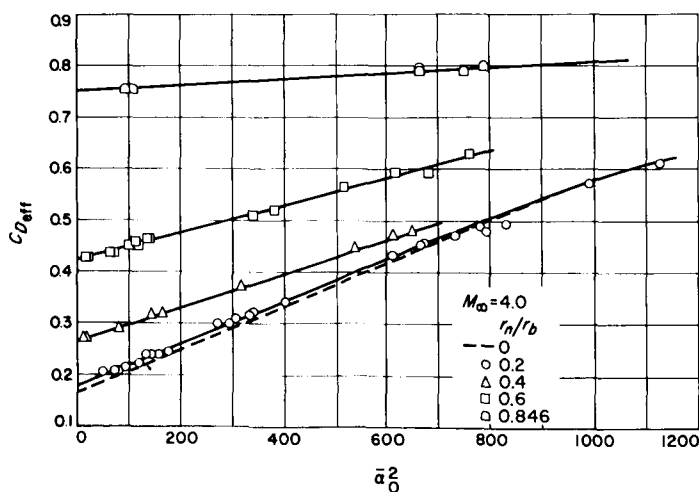


Fig. 26. Effects of nose bluntness on drag

blunt cones the damping coefficient remained constant over the entire Reynolds number range.

Experimental data at a free-stream Mach 8.0 indicate no Reynolds number effects for any of the configurations tested, including the sharp cone. Therefore, increasing both Mach number and nose bluntness ratio, i.e., tending toward a hypersonic flow regime, appears to cause a decrease in variation of dynamic stability with Reynolds number. This conclusion is tentative since the data used for substantiation are sparse. However, a similar effect was noted by Dayman (Ref. 7) when investigating hypersonic viscous effects on the drag of slender cones. His data also showed a decrease in the effects of Reynolds number with an increase in Mach number.

#### D. Drag and Static Stability

Static-stability and free-flight drag data are presented in Figs. 24–37. The drag data are shown in Figs. 24–27, free-flight static-stability data are shown in Figs. 28 and 29, and free-oscillation static-stability data are shown in Figs. 30–37. These data are presented here for information purposes only; no discussion or analysis is included. It should be noted that the data are a by-product of a dynamic-stability investigation and are, in fact, necessary in order to reduce and analyze dynamic-stability data.

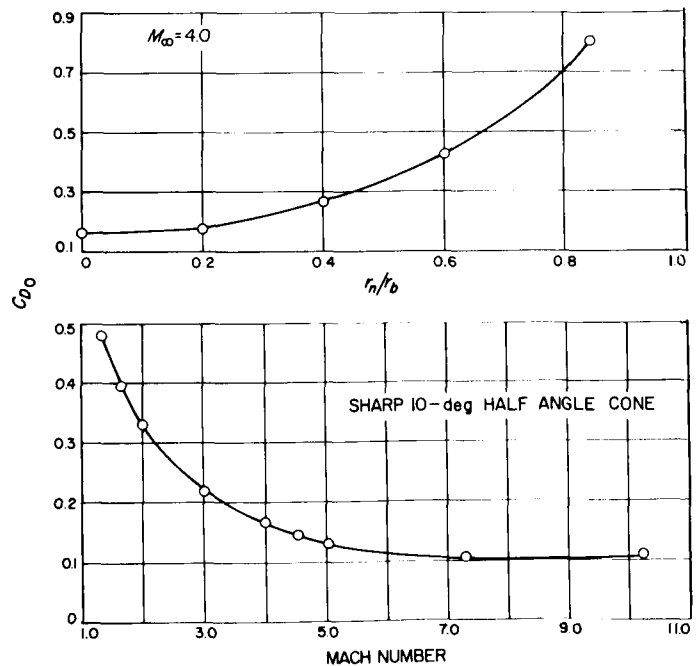


Fig. 27. Effects of nose bluntness and Mach number on drag

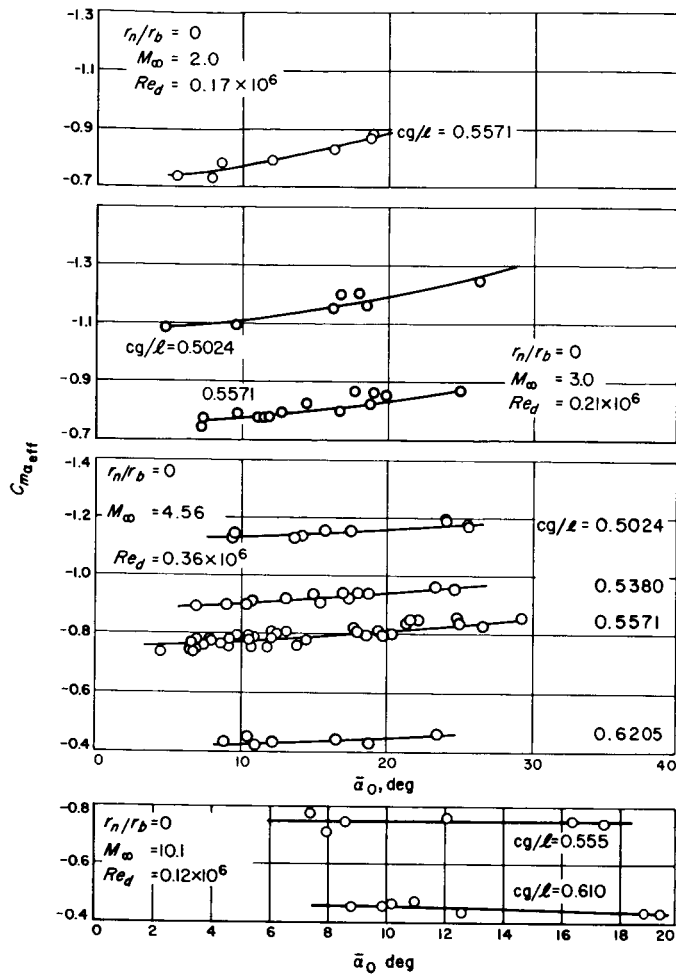


Fig. 28. Free-flight static-stability data: Plot A

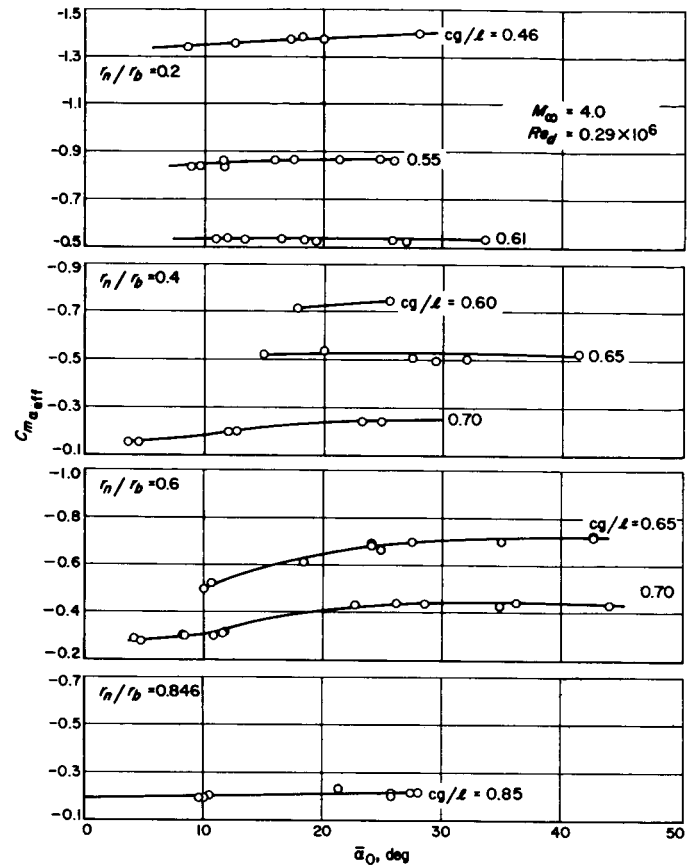


Fig. 29. Free-flight static-stability data: Plot B

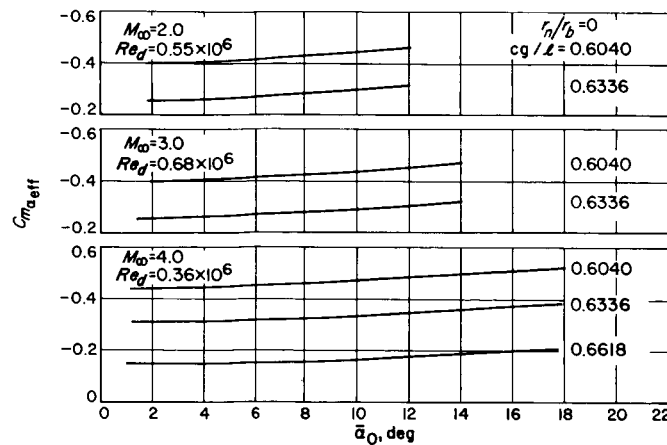


Fig. 30. Free-oscillation static-stability data: Plot A

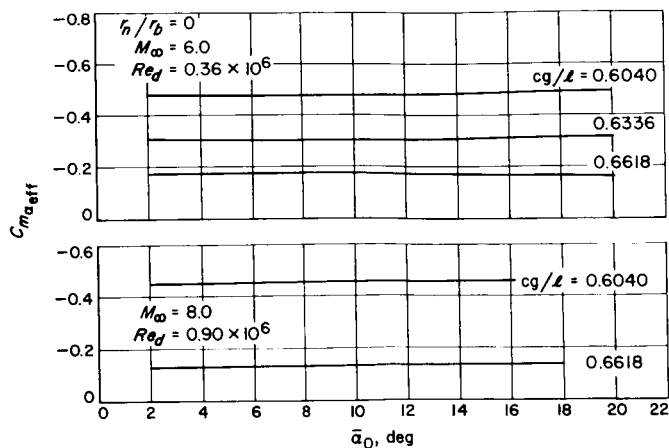


Fig. 31. Free-oscillation static-stability data: Plot B

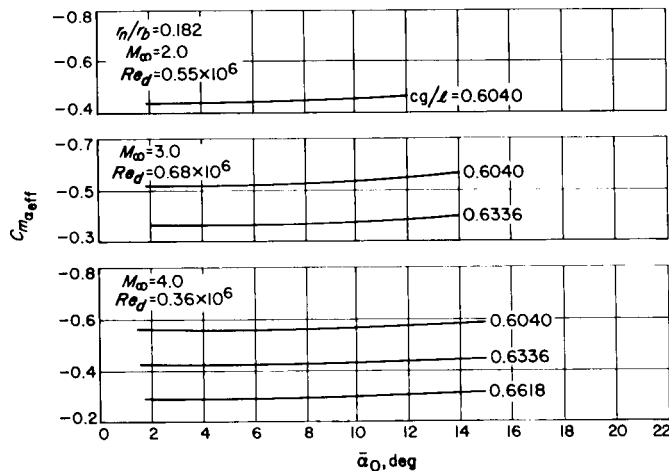


Fig. 32. Free-oscillation static-stability data: Plot C

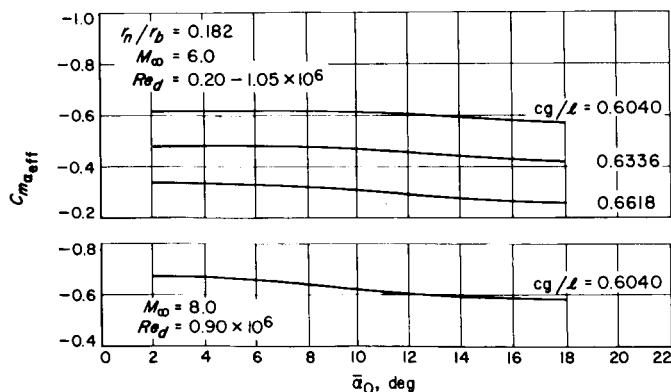


Fig. 33. Free-oscillation static-stability data: Plot D

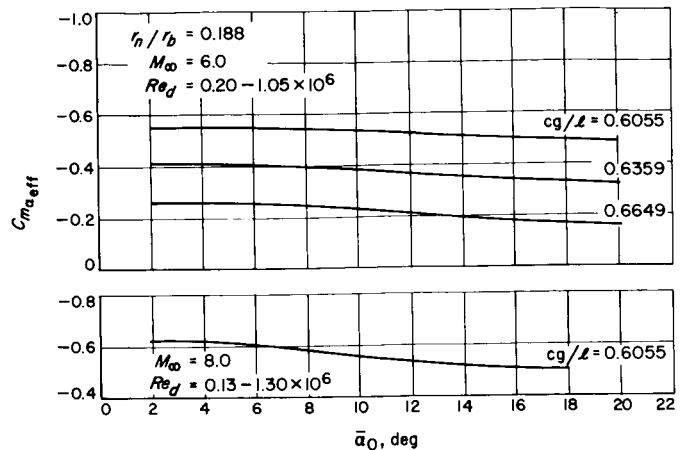


Fig. 34. Free-oscillation static-stability data: Plot E

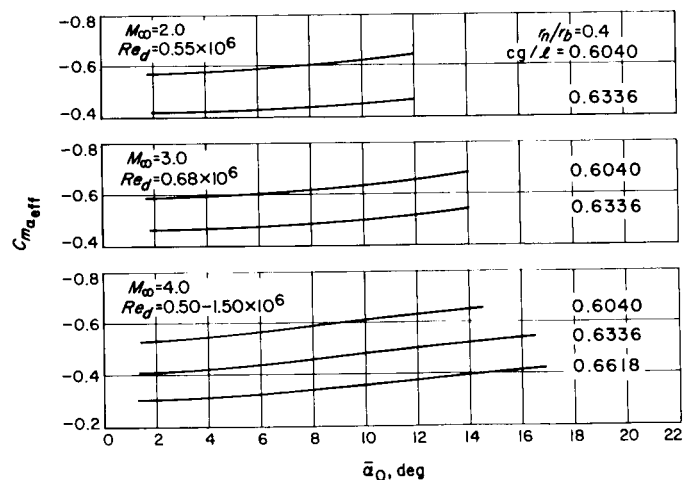


Fig. 35. Free-oscillation static-stability data: Plot F

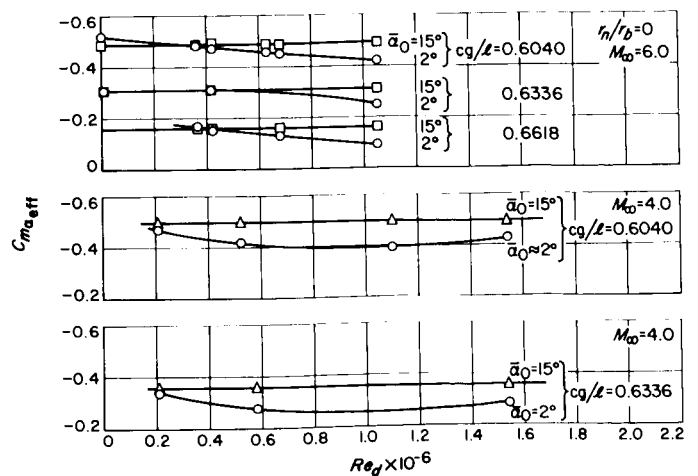


Fig. 36. Effects of Reynolds number on static stability: Plot A

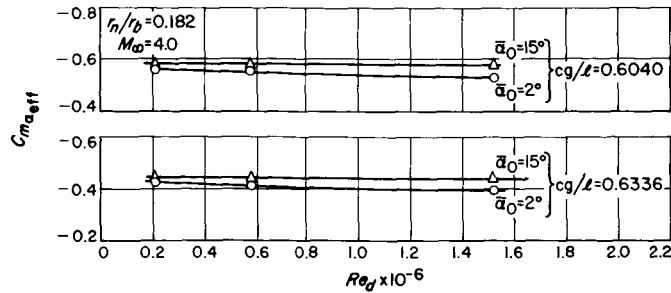


Fig. 37. Effects of Reynolds number on static stability: Plot B

## V. SUMMARY OF RESULTS

A parametric investigation of the dynamic-stability characteristics of a family of spherically blunted 10 deg half-angle cones has been conducted. The parameters considered, other than nose bluntness radius, are oscillation amplitude, center-of-gravity location, Mach number, and Reynolds number. The following discussion includes the major trends observed in the test result.

Dynamic stability decreases with increasing nose bluntness. A sharp cone is considerably more stable than the Newtonian prediction; however, as the bluntness radius increases, the curve converges toward the Newtonian value. For a bluntness ratio  $r_n/r_b = 0.846$ , the Newtonian theory very adequately predicts the stability derivative. For a slender cone, a dynamic-stability vs oscillation-amplitude curve has a characteristic shape; nearly constant at lower amplitudes, an abrupt increase in dynamic stability at an amplitude near the cone half-angle, and a leveling off and asymptotic approach to a new value at the higher amplitudes. This effect becomes

less pronounced as the nose bluntness increases to the point where for the blunter configurations the coefficient remains constant with amplitude. The dependence of dynamic stability on center-of-gravity location is approximated quite well with a linear transformation equation. This approximation applies at all amplitudes, even though the static aerodynamics may be quite nonlinear, when effective coefficients over an oscillation cycle are used in the equation. For a sharp cone, the dynamic stability is highly dependent upon Mach number. Existing theoretical methods adequately predict both the trend and level of the curve. The variation in the coefficient with Mach number is greatly reduced even for a slightly blunted cone. For a very blunt cone there is almost no change with Mach number, and the level is predicted by the Newtonian impact theory. For the sharper shapes, Reynolds number has a significant influence on dynamic stability. Again, the magnitude of this effect decreased with the increasing bluntness ratio. The data also indicate a decrease in Reynolds number effects with an increase in free-stream Mach number.

## NOMENCLATURE

$A$	model reference area, $\pi d^2/4$	$r_b$	model base radius, $d/2$
$cg$	center of gravity; distance to center of gravity from cone vertex	$r_n$	radius of spherical nose bluntness
$C_D$	drag coefficient, drag force/ $q_\infty A$ ; $C_{D_0}$ = drag coefficient at $\alpha = 0$	$Re_d$	free-stream Reynolds number based on model diameter
$C_L$	lift coefficient, lift force/ $q_\infty A$ ; $C_{L_\alpha}$ = lift coefficient slope per radian	$V$	model velocity relative to media
$C_m$	pitching moment coefficient, pitching moment/ $q_\infty A d$ ; $C_{m_\alpha}$ = pitching moment coefficient slope per radian	$X$	model position relative to media
$\{C_{m_q} + C_{m_{\dot{\alpha}}}\}$	effective dynamic stability coefficient (assumed constant over an oscillation cycle) $\partial C_m / \partial(qd/V) + \partial C_m / \partial(\dot{\alpha}d/V)$ per radian	$\alpha$	angle of attack
$C_N$	normal force coefficient, normal force/ $q_\infty A$ ; $C_{N_\alpha}$ = normal force coefficient slope per radian	$\alpha_0$	initial oscillation amplitude
$(C_{N_q} + C_{N_{\dot{\alpha}}})$	$\partial C_N / \partial(qd/V) + \partial C_N / \partial(\dot{\alpha}d/V)$ per radian	$\bar{\alpha}_0$	effective oscillation amplitude
$d$	reference length, model diameter	$\lambda$	damping parameter
$I$	model moment of inertia about a transverse axis at center of gravity	$\rho$	gas density
$m$	model mass	$\omega$	oscillation frequency, radians/sec
$M$	Mach number	$\Omega$	distance oscillation frequency, radians/distance X traveled
$q$	angular pitching velocity	$(\cdot)$	derivative with respect to time
$q_\infty$	free-stream dynamic pressure		

## Subscripts

0	conditions at distance = 0
eff	effective
$x$	conditions at distance = X
$\infty$	free-stream conditions

## REFERENCES

1. Holway, H. P., Herrera, J. G., and Dayman, B., Jr., *A Pneumatic Model Launcher for Free-Flight Testing in a Conventional Wind Tunnel*, Technical Memorandum 33-177, Jet Propulsion Laboratory, Pasadena, Calif., July 30, 1964.
2. Prislin, R. H., *Free-Flight and Free-Oscillation Techniques for Wind-Tunnel Dynamic-Stability Testing*, Technical Report 32-878, Jet Propulsion Laboratory, Pasadena, Calif., March 1, 1966.

**REFERENCES (Cont'd)**

3. Jaffe, P., and Prislín, R. H., "Effect of Boundary-Layer Transition on Dynamic Stability", *J. Spacecraft Rockets*, vol. 3, pp. 46-52, January 1966.
4. Moore, F. K., *Laminar Boundary Layers on Cones in Supersonic Flow at Large Angle-of-Attack*, NACA TN 2844. National Advisory Committee for Aeronautics, Washington, November 1952.
5. Tobak, M., and Wehrend, W. R., *Stability Derivatives of Cones at Supersonic Speeds*, NACA TN 3788. National Advisory Committee for Aeronautics, Washington, September 1956.
6. Saverwein, H., *Application of the Piston Analogy to the Calculation of Stability Derivatives for Pointed Axially-Symmetric Bodies at High Mach Numbers*, Document RAD-TM 61-40. AVCO Corporation, Wilmington, Mass., October 1961.
7. Dayman, B., Jr., "Hypersonic Viscous Effects on Free-Flight Slender Cones", *AIAA J.*, vol. 3, no. 8, pp. 1391-1400, August 1965.